Master's Thesis

Liquefaction potential assessment based on sand boils observed during the 2017 M5.4 Pohang, Korea earthquake

Mirae Kim

Department of Urban and Environmental Engineering
(Disaster Management Engineering)

Graduate School of UNIST

2019

Liquefaction potential assessment based on sand boils observed during the 2017 M5.4 Pohang, Korea earthquake

Mirae Kim

Department of Urban and Environmental Engineering

(Disaster Management Engineering)

Graduate School of UNIST

Liquefaction potential assessment based on sand boils observed during the 2017 M5.4 Pohang, Korea earthquake

A thesis submitted to the Graduate School of UNIST
in partial fulfillment of the requirements for the degree of
Master of Science

Mirae Kim

07. 10. 2019
Approved by

_____

Advisor
Byungmin Kim

Liquefaction potential assessment based on sand boils observed during the 2017 M5.4 Pohang, Korea earthquake

Mirae Kim

This certifies that the thesis of Mirae Kim is approved.

07/10/2019

_____

Advisor: Byungmin Kim
Department of Urban and Environmental Engineering
Ulsan National Institute of Science and Technology (UNIST)

_____

Thesis Committee Member: Young Joo Lee
Department of Urban and Environmental Engineering
Ulsan National Institute of Science and Technology (UNIST)

_____

Thesis Committee Member: Han-saem Kim
Earthquake Research Center
Korea Institute of Geoscience and Mineral Resources (KIGAM)

ABSTRACT

The M5.4 earthquake occurred on November 15, 2017 in Heunghae eup, Pohang city. This earthquake was recorded as the second largest instrumented earthquake in South Korea and caused numerous damages on grounds and structures. Unlike the 2016 **M**5.5 Gyeongju, South Korea earthquake, the strongest instrumented earthquake, the Pohang earthquake occurred in the area of Quaternary sediments with thick infilling and alluvial strata, resulting in greater damages due to ground motion amplifications and liquefaction. Among the other ground deformations such as settlements, cracks, and landslides, the hundreds of liquefaction-induced sand boils observed near the epicenter were the major issue. Korea Institute of Geoscience and Mineral Resources (KIGAM) recorded locations of those sand boils. This study collected around 2,000 Standard Penetration Test (SPT) N values from the Geotechnical Information Portal System, the National Disaster Management Research Institute, the Korea Meteorological Administration and local government offices. The peak ground acceleration (PGA) obtained from the U.S. Geological Survey (USGS) Shake map. This study computed Liquefaction Potential Index (LPI) and Liquefaction Severity Number (LSN) using those data. It turned out that the higher LPI and LSN values correspond with the locations of sand boil occurrence. This study evaluated the computed LPI and LSN based on accuracy. LPI has 69.5% accuracy, and LSN has 67.5% accuracy. In addition, this study calculated the probability using the number of girds where sand boil occurred and no sand boil is observed. The liquefaction probabilities are approximately 0.2 and 0.4 when the LPIs are 5 and 15, respectively. The liquefaction probabilities are approximately 0.1 and 0.3 when the LSNs are 30 and 70, respectively. Furthermore, this study computed the geospatial liquefaction probability model using the locations of sand boil and the influencing factors reflecting the ground motion intensities and geological and soil characteristics (i.e., peak ground acceleration (PGA), peak ground velocity (PGV), compound topographic index (CTI) from the digital elevation model (DEM), average SPT-N value for the top 5m soil deposits, distance to river near the locations of sand boil, V_{S30} and depth to rock). The liquefaction probability model was derived through logistic regression. The proposed probability model has 76% accuracy.

Table of Contents

LIST OF FIGURES

LIST OF TABLES

1. INTRODUCTION

Korea is known for safety area from the earthquake compared to the neighboring countries, Japan and China. Frequency of occurrence and the magnitude of earthquake are low it because Korea is located in the Eurasian plate. Since the 1978 when the earthquake observation, the biggest earthquake has occurred in Gyeong-ju in 2016 and the second biggest earthquake have occurrence in Pohang in 2017. Figure 1(a) shows the active faults in Korea, there are many active faults in Korea (Choi et al. 2012). It means Korea is not a safety area from the earthquake. The M5.4 Earthquake occurred on November 15, 2017 in Heunghae eup, Pohang city, South-Korea. And there were two foreshocks M2.1 and M2.6 seven minutes before the main shock. In addition, Figure 1(b) shows the many aftershocks with magnitudes of 3-4 (KMA 2018). The Pohang earthquake completely changed the public's perception of the earthquake. In addition, the Pohang earthquake caused a lot of structural and geological damage (Kim et al. 2018). Such as building settlement, lateral spreading and liquefaction (KIGAM 2018; Kang et al. 2019). Liquefaction is the first occurrence in Korea.

The sand boils occurred at the time of the Pohang earthquake. It was one of the liquefaction consequences. Liquefaction is a phenomenon where water under the ground rises out of the ground because of the strong earthquake shaking and the ground changes to a liquid state. It commonly occurs in weakly sandy soil or in reclaimed. As a result, buildings and roads on the ground are damaged by settlement and structures such as water pipe under the ground are damaged by leakage, causing severity damage to infrastructure facilities. Gihm et al. (2018) has conducted an extensive survey and identified more than 600 sand boils. Figure 2 shows the example photos of the sand boils.

Finally, this study computed the Liquefaction Potential Index (LPI) and Liquefaction Severity Number (LSN) and compared the location of sand boils in Heunghae eup, Pohang city. Then calculated the accuracy, Cumulative Probability and Probability of the number of the Liquefaction. Furthermore, computed Liquefaction Probability model using geological data of Pohang city.

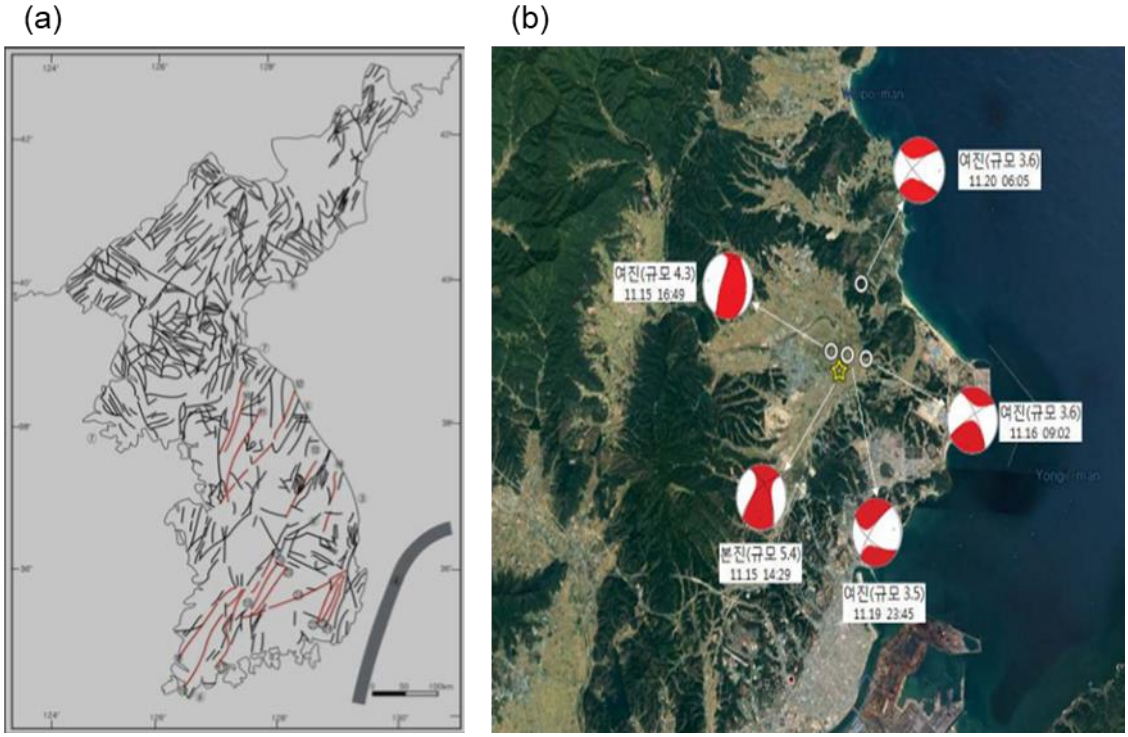

Figure 1 Maps of (a) Korea fault and (b) main shock and aftershocks on Pohang earthquake. (Choi et al. 2012; KMA 2018)

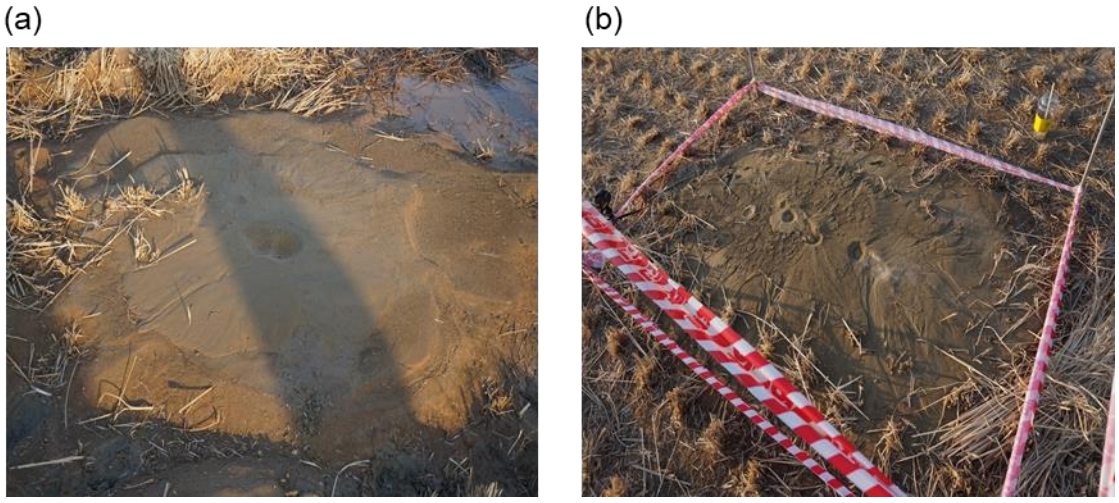

Figure 2 The example photos of Sand boils caused by the 2017 M5.4 Pohang Earthquake.

2. LPI AND LSN

2.1 Previous studies

All over the world, there are many methods to calculate the liquefaction potential. Generally, LPI is representative used and LPI_{ISH} and LSN are used as the next frequently. Methods were classified by using data: Standard Penetration Test (SPT), Cone Penetration Test (CPT) and Shear-wave velocity (V_S). Holzer et al. (2006) calculated the LPI using the 202 seismic CPT soundings and to measuring penetration resistance, shear-wave velocity was measured in each sounding. CPT was used for classification of soil type that soil behavior type index (I_C) described by Robertson (1990) and V_S was used both to know the geological units in soundings and to prepare maps of NEHRP site classes based on 30-m-average velocity (V_{S30}). LPI values were computed for each CPT sounding based on M6.6 and M7.1 earthquake on the nearby Hayward Fault. PGA values were predicted with the ground motion prediction equation of Boore et al. (1997). Then evaluated the liquefaction potential index of surficial geological units for hazard mapping near the eastern shore of Sn Francisco Bay, California, and including the city of Oakland. This research aims to help the users to assess better the liquefaction hazard map when design the land and reviewing investigations in regulatory seismic hazard zones. Sonmez and Ulusay (2008) calculated the LPI with the 1999 Kocaeli earthquake in Turkey (M_W = 7.4) using the 345 Standard Penetration Test (SPT) geotechnical boreholes data. Sonmez and Ulusay (2008) classified boreholes into three groups: <10, 10-15 and >15 m in depth and they ignored the very stiff Pliocene units. As a result, the total boreholes decreased from 345 to 135. This research's study area is the southern coast of Izmit Bay where liquefaction caused by Kocaeli earthquake. PGA values was assumed to 0.35g by using the data that 0.3g was recorded at Yarimca and studied by Cetin et al. (2004) using one-dimensional equivalent linear site response studies said that 0.3-0.4g would be realistic. They said the liquefaction along the southeastern part of Izmit Bay appears to have occurred within the Quaternary deposits at shallow depth. Maurer et al. (2014) calculated the LPI using data from the 2010 to 2011 Canterbury (New Zealand) Earthquake sequence. The data includes the M_W7.1 Darfield earthquake and M_W6.2 Christchurch earthquake as well as 11 other moment magnitude-scale events at M_W5.0 or greater. This study uses the 1,495 Cone Penetration Test (CPT) soundings that were performed in the 18 months after the Darfield earthquake and 322 soundings were removed from this study, leaving a total of 1,173 soundings. Van Ballegooy et al. (2014) calculated the LPI and LSN using the 11,500 CPT soundings with four major Christchurch (New Zealand) earthquakes (Mw 5.6 to 7.1). This researcher compared the LPI and LSN according to the observed land damage.

2.2 Data

This study collected the geological data in Pohang that represents Pohang's geological characters. Many factors that used calculation and evaluation of LPI and LSN are shown in Figure 3. The 2017 Pohang earthquake generated hundreds of sand boils mostly in the rice paddies as shown in Figure 3(a). Because it was November, and the rice plants were already harvested, the liquefaction-induced sand boils were easily observed. The rice paddies where most of the sand boils occurred are within a basin and are surrounded by mountains. This study limited the study area to grid's boundary and include the sand boil that got from the KIGAM (Korea Institute of Geoscience and Mineral Resources). After the Pohang earthquake, KIGAM performed the field work for finding the location, size and characteristic of sand boils. Figure 3(b) shows geology (from the Korea Institute of Geoscience and Mineral Resources (KIGAM)) in the vicinity of the study area. It is worth noting that 97.3 % of sand boils occurred within the Quaternary alluvium. In addition, the sand boils were concentrated near the epicenter: 96.2 % of the sand boils occurred within a 4-km radius from the epicenter, and 80.53 % within a 2-km radius. It is noticeable that the sand boil locations are aligned along rivers (i.e., Gokgang stream and Chogok stream as shown in Figure 3(a). To calculate the Liquefaction probability, collected boring data with Standard Penetration Test (SPT) N value SPT data in Pohang city. A total of 1,913 existing borehole datasets for the Pohang city were obtained from the Geotechnical Information Portal System, the National Disaster Management Research Institute, the Korea Meteorological Administration and local government offices. Locations of the boreholes in the vicinity of the study are shown in Figure 3(c). There are 17 boreholes within the study area. These boreholes and those in the vicinity are used for spatial interpolation to estimate liquefaction severity indices within the study area. The borehole datasets primarily include soil types and SPT *N*-values. Some boreholes have information regarding ground water tables which were used later for liquefaction severity index estimation. Where, 'BH-1', 'BH-2', 'BH-3' and 'BH-4' represents the borehole near the locations of sand boil and locations of non-sand boil. In case of evaluation the liquefaction potential, Magnitude and PGA (Peak Ground Acceleration) is most important factor, so in this study, got the distribution of PGA values from ShakeMap by U.S. Geological Survey (USGS, https://earthquake.usgs.gov/data/shakemap/). Most of the sand boils occurred in the areas with PGA of 0.2 g as shown in Figure 3(d).

Magnitude of earthquake is the important factor to affect the liquefaction occur. There is another factor affecting the liquefaction potential is water table. According to the research, it said decreasing water table make low liquefied material so, it is less the liquefaction potential. (Moss et al. 2017) Like this, water table is significant impact on the liquefaction potential. An average ground water table from the 23 boreholes within the basin (in the study area and its vicinity) that were investigated prior to the 2017 Pohang earthquake is approximately 1.78 m. An average ground water table from the 3 boreholes within the study area that were investigated 5 days after the Pohang earthquake is approximately 0.83

m. It is possible that the ground water table rose after the earthquake. Therefore, a ground water table of 1.5 m was used in this study. Additionally, SPT results represents the N values by depth. When looking at the data, there were many data that were not uniform the thickness. This study corrected the data to 1m interval to compute the liquefaction potential because liquefaction potential depends on the depth. When calculating the LPI and LSN, there are two conditions to consider there is no liquefaction potential in case of (1) over the water table and (2) soil layer include a layer of high plasticity clay.

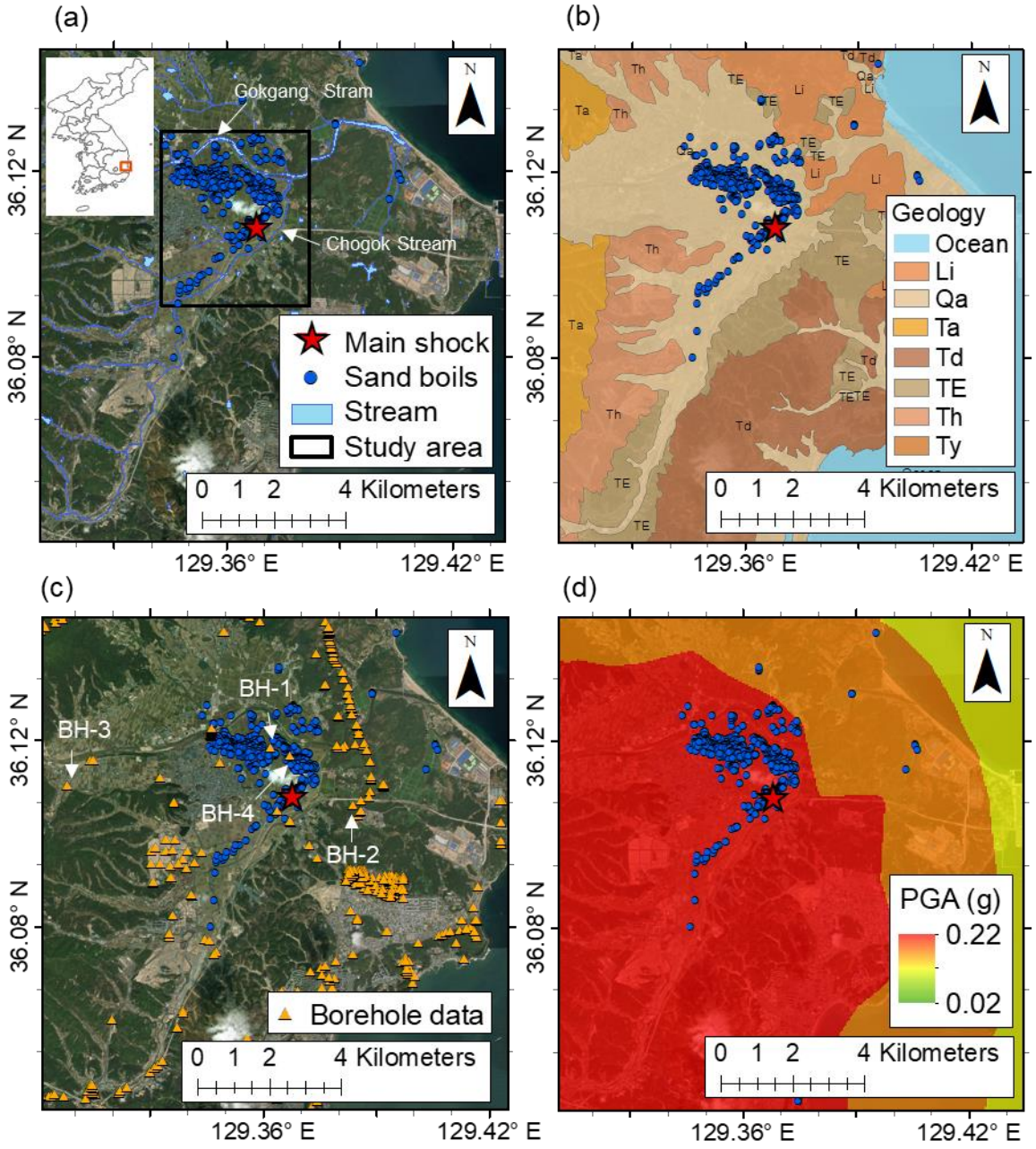

Figure 3 The maps of (a) locations of the 2019 M5.4 Pohang Earthquake main shock epicenter, sand boils near the epicenter and river information near the locations of sand boil. The study area is shown in the insert map;; (b) Geology map (1:50,000 scale) of Pohang city near the study area obtained from the KIGAM (Li: Cretaceous Liparite; Qa: Quaternary Alluvium; Ta : Tertiary Hakrim Formation; Td : Tertiary Duho Formation; TE : Tertiary Idong Formation; Th : Tertiary Heunghae Formation; and Ty : Tertiary Yonam Formation; (c) locations of the borehole data; and (d) map of peak ground acceleration (PGA) estimated by the USGS ShakeMap on Pohang earthquake.

2.3 Methodology

Both LPI and LSN require calculations of cyclic resistance ratio (CRR) and cyclic stress ratio (CSR). This study estimated CRR based on Idriss and Boulanger (2004) and Idriss and Boulanger (2008). SPT N-values corrected based on the recommendation by the National Center for Earthquake Engineering Research (NCEER) Working Group (Youd and Idriss 2001; Seed et al. 2003; Cetin et al. 2018). Vertical stresses were calculated using typical unit weight values of soils: 18 kN/m^3 for silts and clays; 20 kN/m^3 for sands; and 21 kN/m^3 for gravels (Coduto et al. 2011). A unit weight of 20 kN/m^3 was used when a soil type is unknown.

$CRR_{7.5}$ is taken Idriss and Boulanger (2004) and Idriss and Boulanger (2008) as

$$CRR_{7.5} = \exp\left(\frac{(N_1)_{60cs}}{14.1} + \left(\frac{(N_1)_{60cs}}{126}\right)^2 - \left(\frac{(N_1)_{60cs}}{23.6}\right)^3 + \left(\frac{(N_1)_{60cs}}{25.4}\right)^4 - 2.8\right) \quad (1)$$

where $(N_1)_{60cs} = (N_1)_{60} + \Delta(N_1)_{60}$, $(N_1)_{60}$ is the value that corrected N value and $\Delta(N_1)_{60}$ is the equivalent clean sand adjustment.

$(N_1)_{60}$ values as

$$(N_1)_{60} = N_1 C_R C_S C_B C_E \quad (2)$$

where C_R is correction factor for rod length, C_S is correction factor for non-standardized sampler configuration, C_B is correction factor for borehole diameter, and C_E is correction factor for hammer energy and C_E is correction factor for hammer energy ratio as shown in Table 1. (Youd and Idriss 2001; Seed et al. 2003)

$N_1 = N \cdot C_N$

where C_N is taken Liao and Whitman (1986) as

$$C_N = \left(\frac{1}{\sigma_V}\right)^{0.5}$$

where $\sigma_V{}'$ is the effective vertical stress at the depth of the SPT in atmosphere.

$\Delta(N_1)_{60}$ is expressed as,

$$\Delta(N_1)_{60} = \exp\left(1.63 + \frac{9.7}{FC + 0.01} - \left(\frac{15.7}{FC + 0.01}\right)^2\right) \quad (3)$$

where FC is Fine Contents in percent. It is 50 for clay and silt and 0 for sand, gravel and rock.

Table 1 Recommended Correction for SPT Equipment Energy and Procedures (Youd and Idriss 2001; Seed et al. 2003)

<table>
<tr><td>C_R</td><td>
<table>
<tr><td>Rod Length</td><td>C_R</td></tr>
<tr><td>< 3m</td><td>0.75</td></tr>
<tr><td>3 – 4m</td><td>0.80</td></tr>
<tr><td>4 – 6m</td><td>0.85</td></tr>
<tr><td>6 – 10m</td><td>0.95</td></tr>
<tr><td>10 – 30m</td><td>1.00</td></tr>
</table>
</td></tr>
<tr><td>C_S</td><td>For samplers with an indented space for interior liners, but with liners omitted during sampling,
$$C_s = 1 + \frac{N_{1,60}}{100}$$
With limits as $1.10 \leq C_s \leq 1.30$.</td></tr>
<tr><td>C_B</td><td>
<table>
<tr><td>Borehole diameter</td><td>Correction</td></tr>
<tr><td>65 – 115 mm</td><td>1.00</td></tr>
<tr><td>150 mm</td><td>1.05</td></tr>
<tr><td>200 mm</td><td>1.15</td></tr>
</table>
</td></tr>
<tr><td>C_E</td><td>$$C_E = \frac{ER}{60}$$
where ER (Efficiency ratio) is the fraction or percentage of the theoretical SPT impact hammer energy actually transmitted to the sampler, expressed %.
• The best approach is to directly measure the impact energy transmitted with each blow. When available, direct energy measurements were employed.
• The next best approach is to use a hammer and mechanical hammer release system that has been previously calibrated based on direct energy measurements.
• Otherwise, ER must be estimated. For good field procedures, equipment and monitoring, the following guidelines are suggested: Equipment
<table>
<tr><td></td><td>Approximate ER (See Note c))</td><td>C_E (See Note c))</td></tr>
<tr><td>Safety hammer[a)]</td><td>0.4 to 0.75</td><td>0.7 to 1.2</td></tr>
<tr><td>- Donut hammer[a)]</td><td>0.3 to 0.6</td><td>0.5 to 1.0</td></tr>
<tr><td>- Donut hammer[b)]</td><td>0.7 to 0.85</td><td>1.1 to 1.4</td></tr>
<tr><td>-Automatic-Trip hammer (Donut or Safety Type)</td><td>0.5 to 0.8</td><td>0.8 to 1.4</td></tr>
</table>
• For lesser quality fieldwork (e.g.: irregular hammer drop distance, excessive sliding friction of hammer on rods, wet or worn rope on cathead, etc.) further judgement adjustments are needed.</td></tr>
</table>

Notes:

a) Based on rope and cathead system, two turns of rope around cathead, "normal" release (not Japanese "throw"), and rope not wet or excessively worn.

b) Rope and cathead with special Japanese "throw" release. (See also Note [d])

c) For the ranges shown, values roughly central to the mid-third of the range are more common than outlying values, but ER and C_E can be even more highly variable than the ranges shown if equipment and/or monitoring and procedures are not good.

d) Common Japanese SPT practice requires additional corrections for borehole diameter and for frequency of SPT hammer blows. For "typical" Japanese practice with rope and cathead, donut hammer, and the Japanese "throw" release, the overall product of $C_E \times C_B$ is typically in the range of 1.0 to 1.3.

$CRR_{7.5}$ is corrected using the magnitude scaling factor (MSF) and Overburden correction factor (K_σ) to get a CRR_M.

$$CRR_M = CRR_{7.5} \times MSF \times K_\sigma \tag{4}$$

The MSF for sands and clay was proposed by Idriss (1999) and for clay used by Idriss and Boulanger (2008)was developed by Boulanger and Idriss (2007).

$$\begin{aligned} \text{MSF} &= 6.9 \exp\left(\frac{-M}{4}\right) - 0.058 \le 1.8 \quad for\ Sand \\ \text{MSF} &= 1.12 \exp\left(\frac{-M}{4}\right) + 0.828 \le 1.13 \quad for\ Clay \end{aligned} \tag{5}$$

The overburden correction factor, K_σ was developed by Boulanger (2003). Idriss and Boulanger (2008) recommended that the K_σ relationship be expressed as:

$$\begin{aligned} K_\sigma &= 1 - C_\sigma \ln\left(\frac{\sigma'_v}{P_a}\right) \le 1.1 \\ C_\sigma &= \frac{1}{18.9 - 2.55\sqrt{(N_1)_{60cs}}} \le 0.3 \end{aligned} \tag{6}$$

The earthquake-induced cyclic stress ratio, CSR is proposed by Seed and Idriss (1967).

CSR is expressed as:

$$\text{CSR} = 0.65\left(\frac{a_{max}}{g}\right)\left(\frac{\sigma_V}{\sigma_V'}\right)(r_d) \tag{7}$$

where σ_V is the total vertical stress at depth; σ_V' is the effective vertical stress at the depth, a_{max} is the peak acceleration of each layer, g is gravity, r_d is determined using the equation by Idriss (1999).

$$r_d = \exp[\alpha(z) + \beta(z) \cdot M] \tag{8}$$

$$\alpha(z) = -1.012 - 1.126\sin\left(\frac{z}{11.73} + 5.1333\right) \tag{8a}$$

$$\beta(z) = 0.106 + 0.118\sin\left(\frac{z}{11.28} + 5.142\right) \tag{8b}$$

where z = depth blow the ground surface in meters.

Factor of Safety determined by the ratio of CSR (Cyclic Stress Ratio) to CRR (Cyclic Resistance Ratio). Factor of safety is taken by Seed and Idriss (1971)

$$\mathrm{FS}_{liquefaction} = \frac{CRR_M}{\mathrm{CSR}} \tag{9}$$

2.4 LPI

Iwasaki (1978) and Iwasaki et al. (1982) proposed a liquefaction potential index (LPI) that that accounts for thicknesses of liquefiable layers and factors of safety:

$$\text{LPI} = \int_0^{20m} F(z)W(z)\, d_z \tag{10}$$

where F is the function of a factor of safety ($F=1-FS^{liq}$ for $FS^{liq} < 1.0$ and 0 for $FS^{liq} \geq 1$), *W* is the weight function ($W = 10-0.5z$ for $z \leq 20$m and 0 for $z > 20$m), and *z* is the depth. F×W is calculated at every 1 meter and is added for the top 20-m soil deposits that are liquefiable. For non-liquefiable layers, FS^{liq} is considered to be greater than 1, resulting in $F(z) = 0$. Note that the LPI is inversely proportional to FS^{liq} and depth and is commensurate with the thickness of a liquefiable stratum where the FS^{liq} smaller 1.0.

LPI values range from 0 to 100 and degree of liquefaction damage according to the LPI range shown in the table below.

Table 2 Degree of damage according to the LPI range (Iwasaki et al. 1982)

LPI Range	Degree of damage
0	No damage
0 < LPI <5	Minor damage
5 < LPI < 15	Major damage
15 < LPI	Severe damage

2.5 LSN

The liquefaction severity number (LSN) is newly developed by Tonkin and Taylor (2013) based on the liquefaction observation from the Canterbury Earthquake Sequence, which is defined:

$$\text{LSN} = 1000 \int_0^{20m} \frac{\varepsilon_v}{z}\, dz \tag{11}$$

where ε_v is the volumetric strain for liquefiable soil layers, which can be estimated based on the Tokimatsu and Seed (1987) procedure and it represents in Figure 4. The strain calculation techniques consider strains that occur where materials have a calculated triggering FS^{liq} that reduces below 2.

The Figure 4 that was proposed by Tokimatsu and Seed (1987) is based on CSR7.5.

Table 3 gives the relative values of stress ratio required to cause liquefaction for earthquake of different magnitudes to the stress ratio required to cause liquefaction for a M = 7.5 event. Thus, by multiplying the r_m values in $CSR_{7.5}$. (Tokimatsu and Seed 1987)

$$CSR_{M=7.5} = CSR_{M=M} \times \frac{1}{r_m} \tag{12}$$

where r_m is the scaling factor for stress ratios (Table 3).

Table 3 Scaling factors for effect of earthquake magnitude on Cyclic Stress Ratio Causing Liquefaction (Tokimatsu and Seed 1987)

Earthquake magnitude, M	Number of representative cycles at 0.65_{max}	Scaling factor for stress ratio, r_m
$8\frac{1}{2}$	26	0.89
$7\frac{1}{2}$	15	1.0
$6\frac{3}{4}$	10	1.13
6	5	1.32
$5\frac{1}{4}$	2-3	1.5

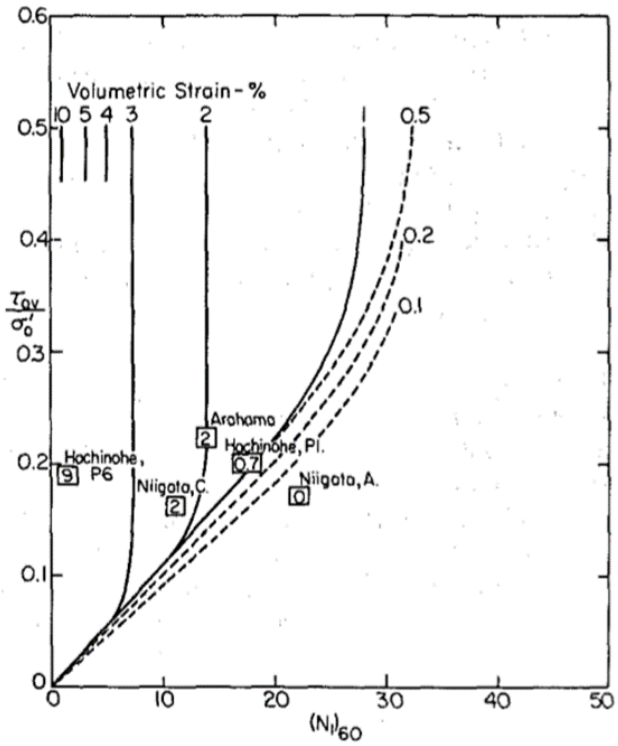

Figure 4 Proposed relationship between Cyclic Stress Ratio ($CSR_{7.5}$) and (N1)60. (Tokimatsu and Seed 1987)

Degree of liquefaction damage according to the LSN range shown in the table below.

Table 4 Degree of damage according to the LSN range (Van Ballegooy et al. 2013)

LSN Range	Degree of damage
0 < LSN < 20	Minor damage
20 < LSN < 40	Major damage
40 < LSN	Severe damage

2.6 Results

Figure 5 (a and b) show examples of the N- and corrected N-values ($N_{1,60}$) for BH-1 (the location is shown in Figure 3). BH-1 is located within the liquefied area (Figure 3) and is composed of silts, sands, and lean clays with small N-values (<20), underlain by gravels, mudstones, and weathered rocks. The CRR values are smaller than 0.6 within a depth of 15 m (Figure 5c). On the other hand, the N-values are greater than 30 at shallow depths (<6m) below which they reach 50 in BH-2 where soils are mixture of silts and gravels (Figure 6). Because the CRR is greater with $N_{1,60}$, CRR was not shown in the panel (Boulanger and Idriss 2014). Figure 7 (a and b) show examples of the N- and corrected N-values ($N_{1,60}$) for BH-3. BH-3 located far away from the liquefied area (Figure 3) and composed of clay and sand with small N-values (<20), underlain by gravels, silt and weathered rocks. The CRR values are smaller than 0.6 within a depth of 7 m (Figure 7c). Figure 8 (a and b) show examples of the N- and corrected N-values ($N_{1,60}$) for BH-4 (the location is shown in Figure 3. BH-4 located within the liquefied area (Figure 3) and is composed of silty sand, gravel and clay with small N-values (<20), underlain by gravel and soft rock. The CRR values are smaller than 0.6 within a depth of 10 m (Figure 8c).

CSR was estimated based on Seed and Idriss (1971) with stress reduction coefficient proposed by Idriss (1999). The peak ground acceleration (PGA) values from ShakeMap by U.S. Geological Survey (USGS, https://earthquake.usgs.gov/data/shakemap/) were used as a_{max}. Most of the sand boils occurred in the areas with PGA of 0.2 g as shown in Figure 3(d). Because the study is narrow (i.e., approximately within a radius of 2 km from the epicenter), the effect of PGA on liquefaction potential would be minor.

Factor of safety against liquefaction can calculated as FS^{liq} = CRR/CSR. The FS^{liq} for BH-1 is smaller than unity at various depths as shown in Figure 5(d). Consequently, LPI and LSN are calculated as approximately 16 and 104, respectively, for BH-1. The FS^{liq} for BH-2 was greater than 1 because CRR greater with $N_{1,60}$. In this case, LPI and LSN are both considered to be zero. The FS^{liq} for BH-3 also over the 1. In this case, LPI and LSN are calculated as approximately 1 and 10, respectively. The FS^{liq} for BH-4 is smaller than unity at various depths. LPI and LSN are calculated as approximately 19 and 135, respectively, for BH-4.

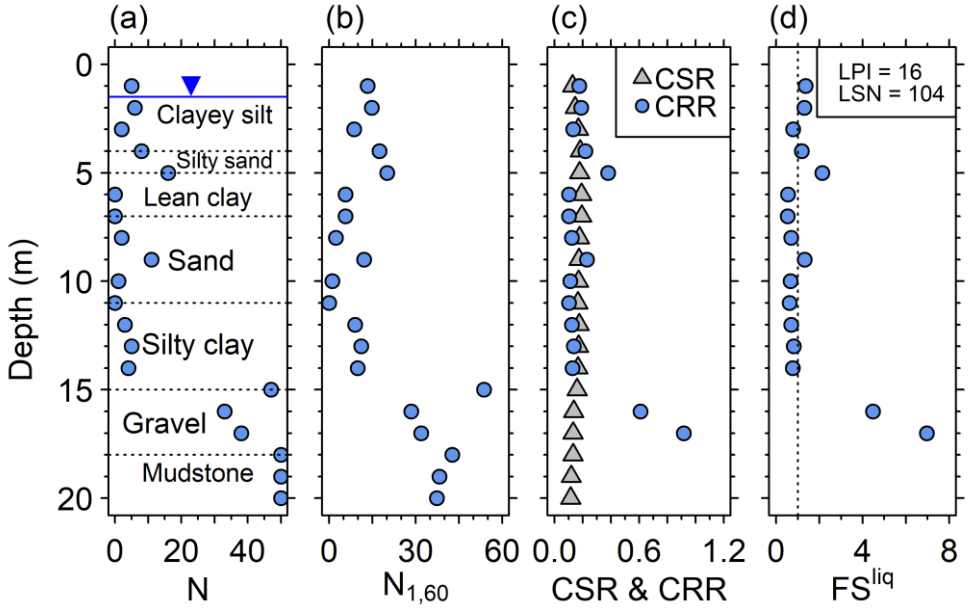

Figure 5 Factors used in the LPI calculation near liquefaction occurred locations at BH-1: (a) raw SPT N-value with strata; (b) corrected N-value ($N_{1,60}$); (c) cyclic stress ratio (CSR) and cyclic resistance ratio (CRR); (d) factor of safety against liquefaction (FS^{liq}).

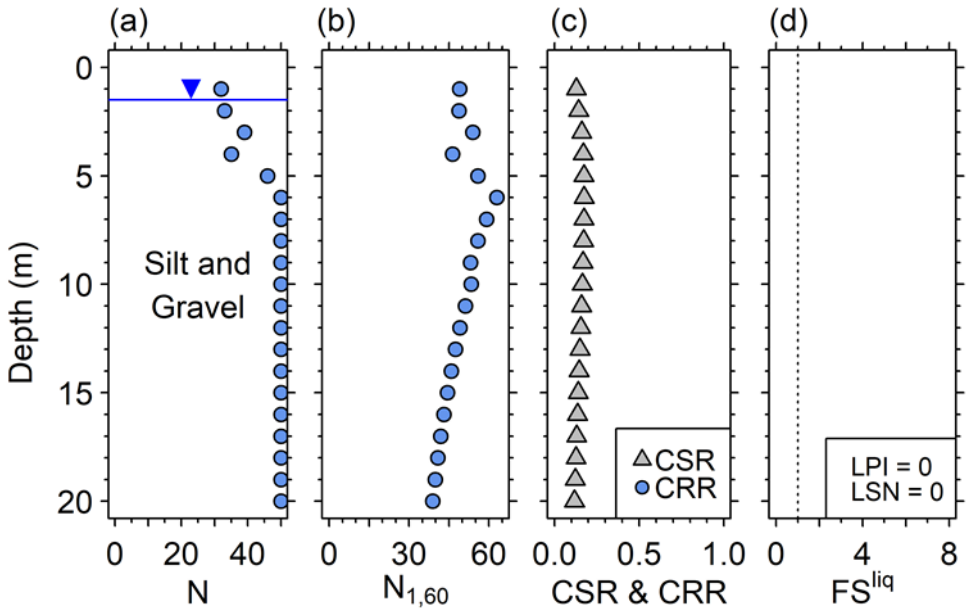

Figure 6 Factors used in the LPI calculation at non-liquefaction occurred locations at BH-2: (a) raw SPT N-value with strata; (b) corrected N-value ($N_{1,60}$); (c) cyclic stress ratio (CSR) and cyclic resistance ratio (CRR); (d) factor of safety against liquefaction (FS^{liq}).

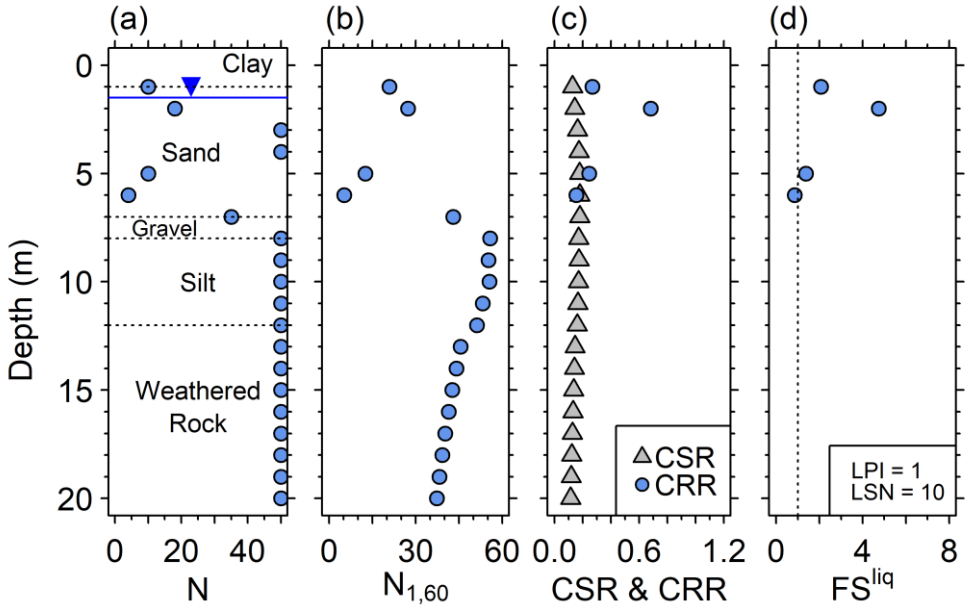

Figure 7 Factors used in the LPI calculation at little liquefaction occurred locations at BH-3: (a) raw SPT N-value with strata; (b) corrected N-value ($N_{1,60}$); (c) cyclic stress ratio (CSR) and cyclic resistance ratio (CRR); (d) factor of safety against liquefaction (FS^{liq}).

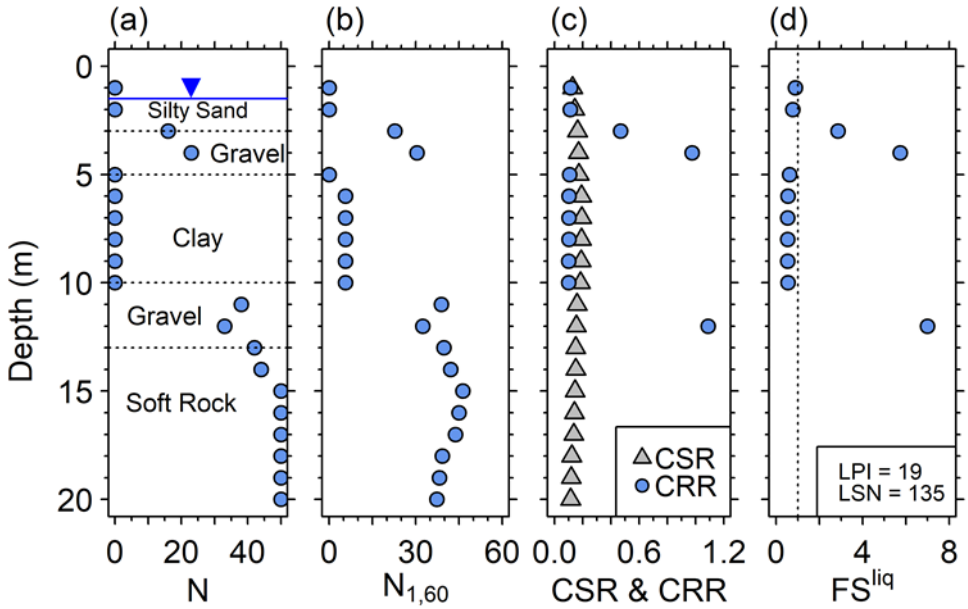

Figure 8 Factors used in the calculation near liquefaction occurred locations at BH-4: (a) raw SPT *N*-value with strata; (b) corrected *N*-value ($N_{1,60}$); (c) cyclic stress ratio (CSR) and cyclic resistance ratio (CRR); (d) factor of safety against liquefaction (FS^{liq}).

LPI and LSN values were estimated at all the borehole locations as shown in Figure 9. The spatial interpolation was conducted with the Inverse Distance Weighted (IDW) method (Shepard 1968) to estimate LPI and LSN values for the areas where no borehole data are available. LPI values were calculated to be high at two boreholes (i.e., 16 and 19) located in the center of the basin (inside the study area). However, LPI values at the edge of basin are zero. Therefore, the spatial interpolation resulted in highest LPI values concentrated in the center of the basin, which are consistent with spatial distribution of sand boil observations (Figure 9a). A similar pattern can be observed for LSN: LSN is highest in the center of the basin (i.e., 135) and approaches zero towards the edge of the basin, also consistent with the sand boil distribution (Figure 9b). Unlike the case of LPI, some boreholes at the edge of the basin have non-zero LSN values, resulting in wider areas with non-zero LSN within the basin.

In order to check the predictive power of LPI and LSN values, a total of 1,600 grid squares (110m×130m size) were developed within the study area that covers approximately 23 km^2 Subsequently, the spatially interpolated LPI and LSN values were averaged and assigned to the grids. Each grid was classified as "liquefied" and "nonliquefied" based on sand boil observations. In that, if there were more than one sand boils within the grid, it was classified as "liquefied". If no sand boil was observed, the grid was classified as "nonliquefied". It is considered that smaller grids are not necessary because the borehole data are not sense within the study area (neither are the calculated LPI and LSN values). Among the 1,264 grids excluding 336 grids belong to mountain areas, 205 are classified as "liquefied" and 1,059 as "nonliquefied".

Figure 10 shows numbers of grids where at least one sand boil was observed and no sand boil was observed (i.e., "liquefied" and "nonliquefied" grids, respectively) for all the LPI and LSN bins. Mountain areas were obtained from the Forest Space Information Service (http://www.forest.go.kr/) and removed in the statistical analyses. Because coverage areas decrease with LPI and LSN values, the number of both liquefied and nonliquefied grids decrease with LPI and LSN values. However, it is clearly observed that the ratio of liquefied grids and nonliquefied grids generally increase with LPI and LSN values.

Figure 10 also presents cumulative probability of liquefied and nonliquefied grids. Mountain areas were removed in the probability calculation. Approximately 55% of the liquefied grids and 20 % of the nonliquefied grids have estimated LPIs higher than 5 (True Positive and False Positive, respectively). Approximately 8% of the liquefied grids and 2% of the nonliquefied grids have estimated LPIs higher than 15. The mean LPI for the liquefied grids (corresponding to the cumulative probability of 50%) is approximately 6. Iwasaki (1978) and Maurer et al. (2014) reported that the mean LPI for the liquefied sites is 15 and 11, respectively. This discrepancy of the mean LPIs for this study and previous studies might be due to different severities of liquefaction considered in the both studies: the liquefaction observed in this study are mostly, while those by Iwasaki include all kinds of severity (i.e., from marginal to moderate and severe liquefaction). Note that the sand boils considered in this study occurred

on the rice paddies where no pavement or structure exists, resulting in easy detection even if the size is small. Maurer et al. (2014) reported 75% and 50% of sites with marginal liquefaction have LPI values greater than 4 and 8, which is comparable with the mean LPI for liquefied the grids for this study.

Figure 11 shows probabilities of liquefaction against LPI and LSN values. The probability of liquefaction is defined as the percentage of liquefied grids. Mountain areas were removed in the statistical analyses. The probabilities increase with LPI and LSN values.

The liquefaction prediction powers of LPI and LSN were checked by accuracy values as shown in Figure 12. A confusion matrix was developed for the 1,264 grids (excluding grids for mountain areas) with four indices: true positive (liquefaction is occurred and LPI or LSN is greater than the threshold), false positive liquefaction is not occurred but LPI or LSN is greater than the threshold), false negative (liquefaction is occurred but LPI or LSN is smaller than the threshold) and true negative (liquefaction is not occurred and LPI or LSN is smaller than the threshold). These mechanism shows in Table 5.

Table 6 and Table 7 shows the number or four indices according to the threshold values of LPI and LSN, respectively. The threshold values varied from 0 to 19 and 0 to 135 for LPI and LSN, respectively. Then, prediction accuracy was calculated by the average of true positive rate (ratio of a number of true positive grids to a number of liquefied grids) and true negative rate (ratio of a number of true negative grids to a number of nonliquefied grids). It shows in Eq13. The mountain areas were removed in calculating the accuracy values. The maximum accuracy for LPI is 69.5 at an LPI of 4 (Figure 12a), and that for LSN is 67.5 at an LSN of 48 (Figure 12b). These accuracy values are for predicting occurrence of sand boils. One should keep in mind that some places with no sand boil observed could have actually been liquefied because 1) some soil strata could have been liquefied even through sand boils were generated on the ground surface, and 2) some sand boils could have been missed. In addition, this study considered the receiver operation characteristics (ROC) curve to evaluate the LPI and LSN (Figure 13). The upper the graph is, the better model performance is. ROC curve is consisted of true positive rate (ratio of a number of true positive grids to a number of liquefied grids) and false positive rate (ratio of a number of true negative grids to a number of liquefied grids), both of which are expressed in Eq. 14.

$$\text{Accuracy} = \frac{\text{TPratio}\left(=\frac{\text{TP}}{\text{TP}+\text{FN}}\right) + \text{TNratio}\left(=\frac{\text{TN}}{\text{TN}+\text{FP}}\right)}{2} \tag{13}$$

$$\text{True positive rate} = \frac{\text{TP}}{\text{TP}+\text{FN}} \tag{14a}$$

$$\text{False positive rate} = \frac{\text{FP}}{\text{TN}+\text{FP}} \tag{14a}$$

Table 5 Confusion Matrix

		Predicted Class	
		Positive	Negative
Observed Class	Positive	TP	FN
	Negative	FP	TN

Table 6 The number of four indices of LPI in threshold 5, 15

Threshold 5		Predicted Class	
		Positive	Negative
Observed Class	Positive	TP (54)	FN (46)
	Negative	FP (23)	TN (77)
Threshold 15		Predicted Class	
		Positive	Negative
Observed Class	Positive	TP (8)	FN (92)
	Negative	FP (1)	TN (99)

Table 7 The number of four indices of LSN in threshold 48, 108

Threshold 48		Predicted Class	
		Positive	Negative
Observed Class	Positive	TP (60)	FN (40)
	Negative	FP (25)	TN (75)
Threshold 108		Predicted Class	
		Positive	Negative
Observed Class	Positive	TP (8)	FN (92)
	Negative	FP (1)	TN (99)

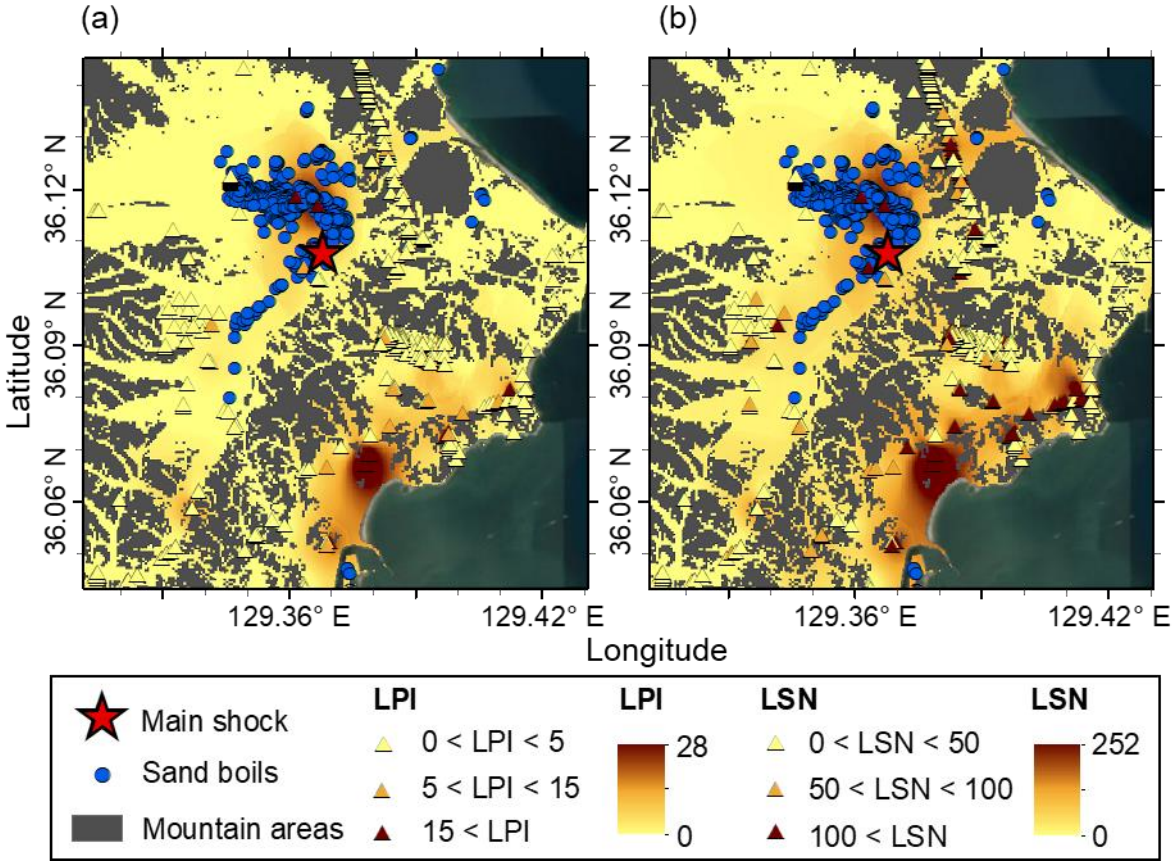

Figure 9 Liquefaction hazard maps for the study area: (a) LPI and (b) LSN.

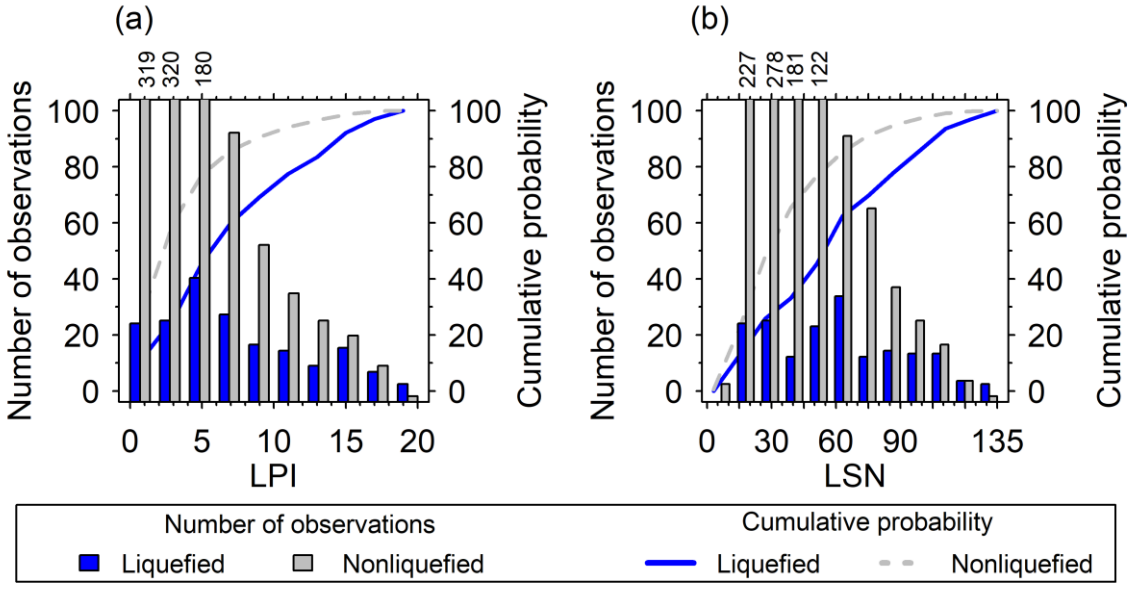

Figure 10 Numbers of sand boil observations and cumulative probabilities of the (a) LPI and (b) LSN. The numbers of sand boil observations not shown in the graph are presented above the panels.

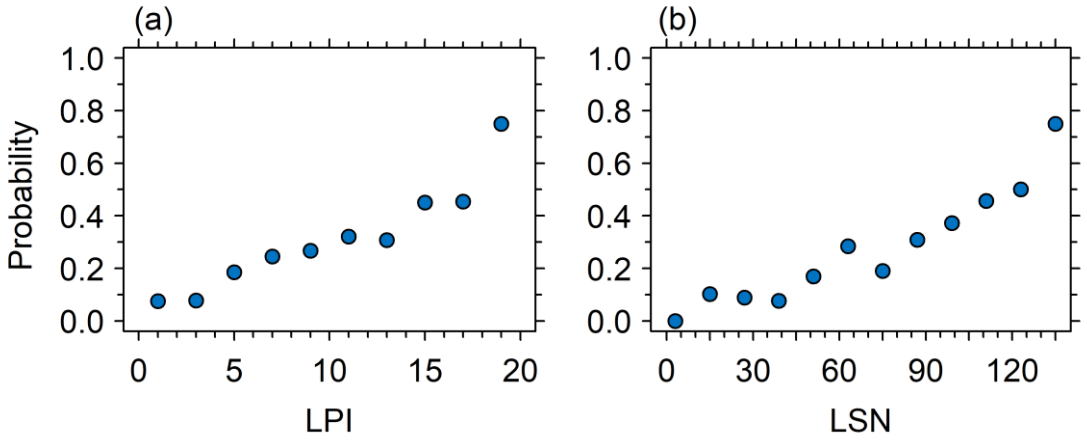

Figure 11 Probabilities of sand boils for each bin of the (a) LPI and (b) LSN.

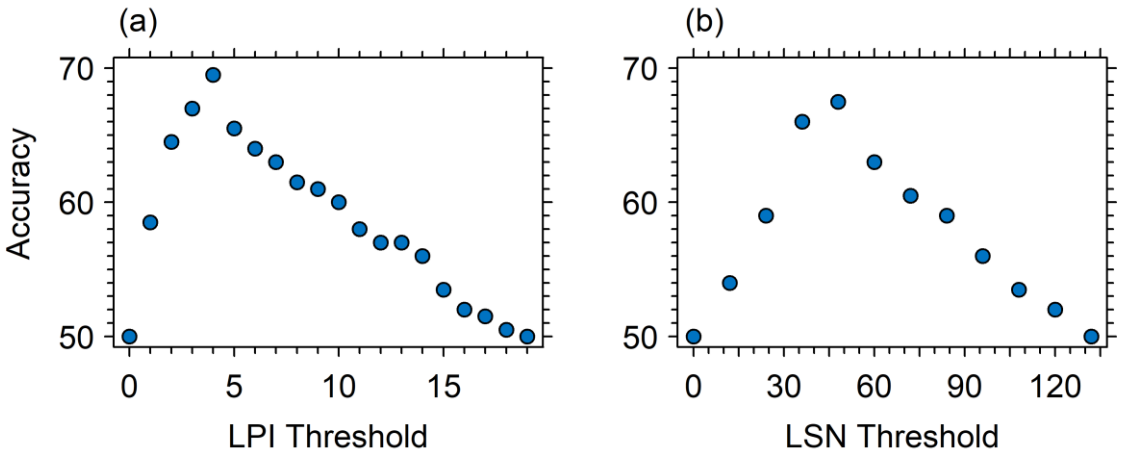

Figure 12 Accuracy of the (a) LPI and (b) LSN with various thresholds.

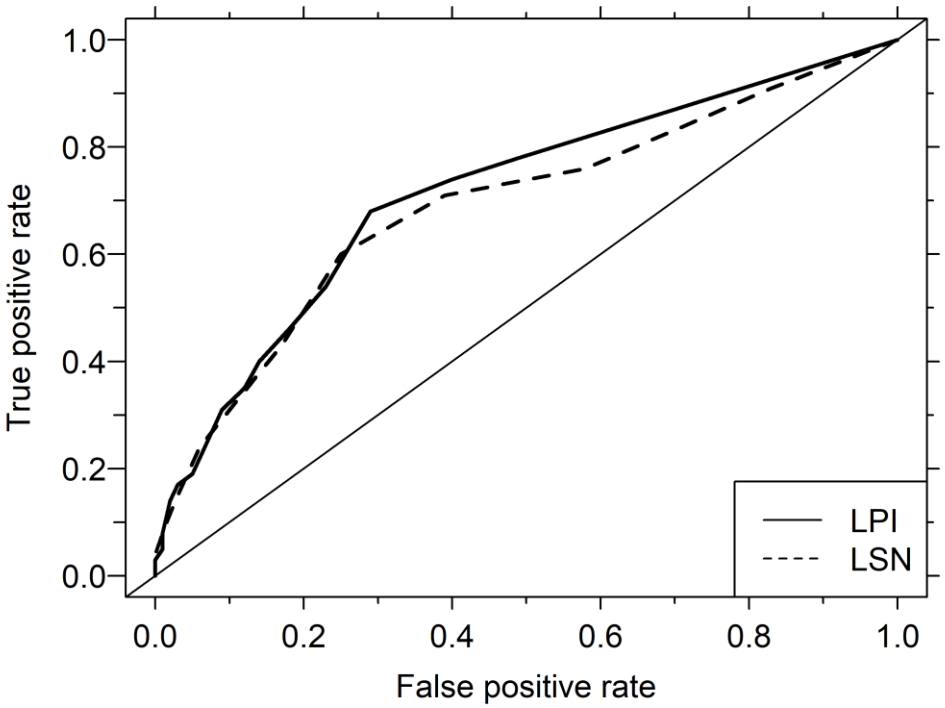

Figure 13 ROC curve of (a) LPI and (b) LSN with one-to-one line.

3. GEOSPATIAL LIQUEFACTION PROBABILITY MODEL

3.1 Previous studies

Zhu et al. (2015) developed a geospatial liquefaction model using the liquefaction observation data from the New Zealand earthquakes (the 2010-2011 **M**7.0-7.1 Christchurch and Darfield earthquake sequence) and the Japanese earthquakes (the 1995 **M**6.9 Hyogo-ken, Nanbu earthquake in Kobe). They considered three broad factors: soils' density, saturation, and dynamic loading. roughness (rock vs. soil), V_{S30} (from topographic slope), dc (distance from the coast), ND (normalized distance) are the density parameters; dc, ND, distance to the nearest river, CTI are the saturation parameters; and PGA from GMPE, PGA from ShakeMap, magnitude scaling factor (MSF) are the dynamic loading parameters. Among the various combinations of parameters for the Nanbu and Christchurch Darfield earthquake data, they derived top performing model which is in a function of $PGA_{M,SM}$, CTI and V_{S30} (Table 8). Zhu et al. (2017) updated the Zhu et al. (2015)'s model by (1) expanding the database to include 27 earthquake from the United States, Japan, New Zealand, China, Taiwan, and India, (2) applying a sampling method to add incomplete datasets, and (3) evaluating new explanatory variables (V_{S30}, elevation, topographic slope, roughness, topographic position index, terrain roughness index, dc and CTI in density parameters, global water table depth, distance to the nearest river, distance to the nearest water body, elevation above the nearest water body, mean annual precipitation and aridity index in saturation parameter and PGA from ShakeMap PGV from ShakeMap, magnitude and magnitude scaling factor (MSF) in dynamic load parameter), and (4) testing interaction terms. Zhu et al. (2017)'s best performing model consisted of PGV, V_{S30}, precipitation, $\sqrt{dc}$, dr and $\sqrt{dc} \times dr$ as shown in Table 8.

Table 8 Liquefaction probability model of previous studies

Proposer	Model name	Models for liquefaction probability (z)
(Zhu et al. 2015)	Regional Model	$Z = 15.83 + 1.443*\ln(PGA_{M,SM}) + 0.136*CTI(30c) - 9.759*ND - 2.764*\ln(V_{S30})$.
(Zhu et al. 2017)	Model 1	$Z = 12.435 + 0.301*\ln(PGV) - 2.615*\ln(V_{S30}) - 5.556 \times 10^{-4} * precip - 0.0287*\sqrt{dc} + 0.0666* dr - 0.0369*\sqrt{dc} \times dr.$

3.2 Data

Figure 14 shows the locations of liquefaction-induced sand boils generated during the Pohang earthquake and the grids in the study area. Mountain areas are also presented. This study selected the study area to include the majority of sand boil observations. The input factors and presence of sand boils are assigned to the 110 × 130 (m) grids which are used in the logistic regression. This study considers various variables inspired by other previous studies Zhu et al. (2015) and Zhu et al. (2017): PGA (peak ground acceleration), PGV (peak ground velocity), CTI (compound topographic index), $\bar{\boldsymbol{N}}^{\boldsymbol{Z}}(Z = 5, 10, 20\ m)$ (average N values to Zm depth), $\boldsymbol{R}^{\boldsymbol{river}}$ (distance to river), V_{SZ} (Z=5, 10, 20, 30 m) (time-averaged shear-wave velocity of the top Z m soil deposits) and $\boldsymbol{D}^{\boldsymbol{rock}}$ (depth to rock as listed in Table 9.

Figure 15 shows maps of the input variables considered in this study. Maps of PGA (peak ground acceleration) and PGV values estimated for the Pohang earthquake were obtained from USGS ShakeMap (https://earthquake.usgs.gov/data/shakemap/) (Figure 15a and Figure 15b). Using the Shuttle Radar Topography Mission (SRTM) DEMs with a 30m resolution (https://earthexplorer.usgs.gov/) CTI is computed as:

$$\text{CTI} = \ln\left(\frac{A}{\tan(\alpha)}\right) \tag{15}$$

where A is the contributing basin area and α is the slope in degrees.

It is well known that the CTI is strongly correlated with soil moisture contents and is a function of both the slope and the contributing basin area. This means that lower CTI values are associated with steeper slope and smaller moisture area, and vice versa. Figure 15(c) shows that the CTI values are higher than 16 in the basin (near the study area), and the mountain areas have lower CTI values. This study calculated the average SPT - N value for the top 5m soil deposits ($\bar{\boldsymbol{N}}^{\boldsymbol{5m}}$) (Figure 15d). Figure 15(e) shows the depths to rock ($\boldsymbol{D}^{\boldsymbol{rock}}$) determined using the collected borehole data that were mentioned in Section 2.2. There are various types of rocks: weathered rock, andesite, tuff tufa, soft rock, conglomerate and clay rock. $\boldsymbol{D}^{\boldsymbol{rock}}$ is the depth to the top of the uppermost rocks. This study used the closest distances to rivers ($\boldsymbol{R}^{\boldsymbol{river}}$). Figure 15(f) shows the rivers near the study area. Lastly, Figure 15(g) shows the V_{S30} near the study area. The $\bar{\boldsymbol{N}}^{\boldsymbol{5m}}$, V_{S30} and $\boldsymbol{D}^{\boldsymbol{rock}}$, which were obtained from the borehole data, were spatially interpolated using the KRIGING tools in GIS program. These data were classified by three categories: ground intensity (peak ground acceleration (PGA) and peak ground velocity (PGV)), soil intensity (average N values ($\bar{\boldsymbol{N}}^{\boldsymbol{5m}}$), shear-wave velocity ($V_{S30}$) and depth to rock ($\boldsymbol{D}^{\boldsymbol{rock}}$) and water contents (compound topographic Index (CTI) and distance to river($\boldsymbol{R}^{\boldsymbol{river}}$)).

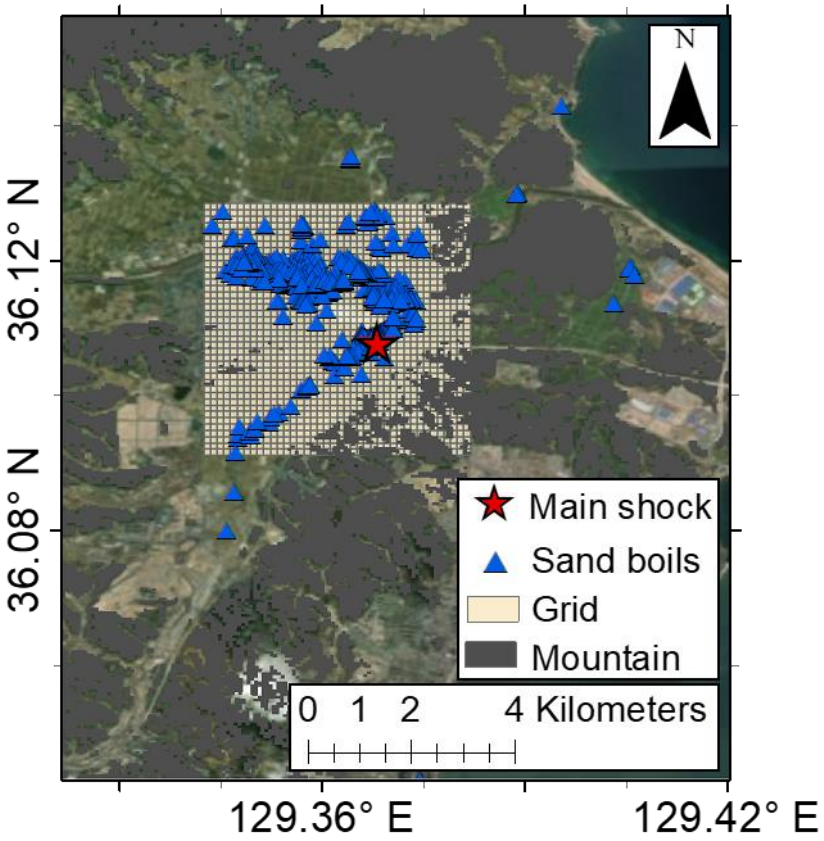

Figure 14 Locations of sand boils, grids within the study area. Mountain areas are shown in gray.

Table 9 Variable input data

Variable Name	Variable Description
PGA	Peak Ground Acceleration
PGV	Peak Ground Velocity
CTI	Compound Topographic Index
$\bar{N}^{Z}(Z = 5, 10, 20\ m)$	Average N values to Zm depth
R^{river}	Distance to River
V_{SZ} (Z=5, 10, 20, 30 m)	Time-averaged shear-wave velocity of the top Z m soil deposits
D^{rock}	Depth to Rock

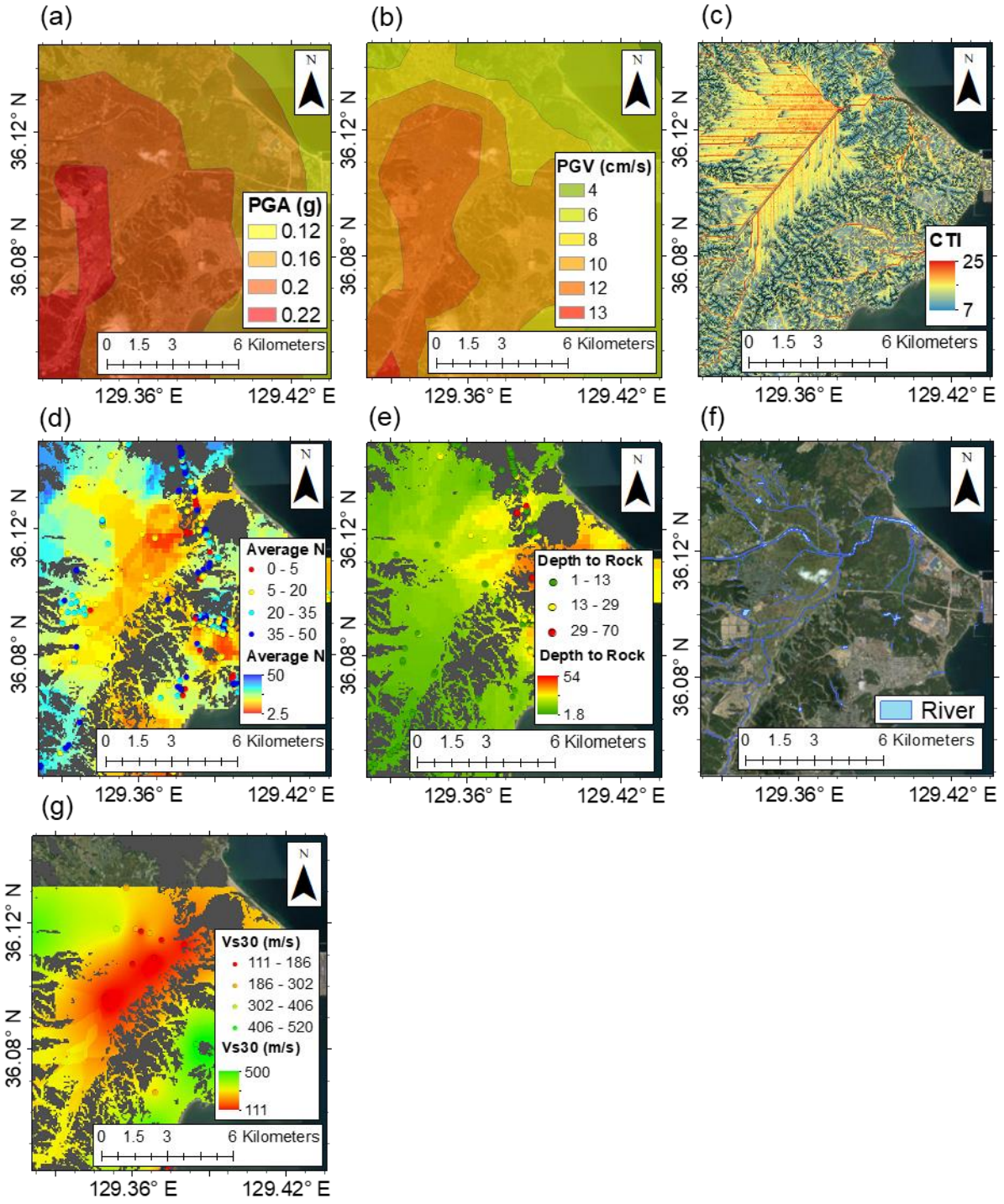

Figure 15 Maps of (a) peak ground acceleration (PGA); (b) peak ground velocity (PGV) values estimated by the USGS ShakeMap; (c) CTI from 30m resolution SRTM; (d) average SPT-N value for the top 5m soil deposits; (e) depths to rock value in Pohang city; and (f) river information in Pohang city; (g) V_{S30}.

3.3 Methodology

This study uses logistic regression to develop a spatial probability model for liquefaction. Logistic regression is a statistical function that describes the relationship between a binary dependent variable (in this case, liquefaction or non-liquefaction) and various independent variables. The logistic regression function is represented in Eq.16 and shows in Figure 16.

$$P(Z) = \frac{1}{1 + e^{-Z}} \tag{16}$$

$Z = \beta_0 + \beta_1 x_1 + \cdots + \beta_k x_k$, $x_1, x_2, \ldots, x_k$ are the explanatory variables, and $\beta_0, \beta_1, \ldots, \beta_k$ are the coefficients calculated from the regression. (16a)

where P is the probability ranging from zero to one.

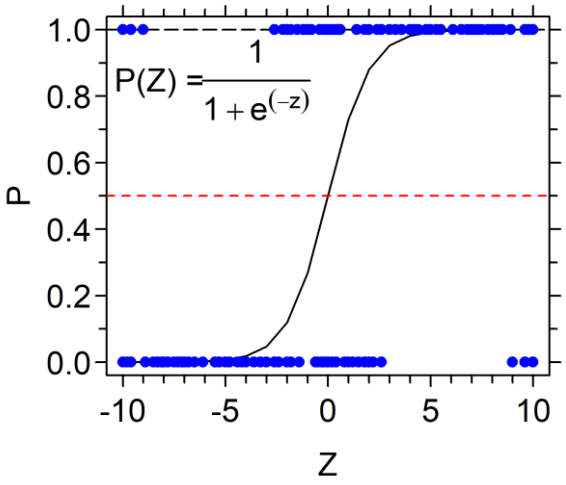

Figure 16 Function of logistic regression

This study inputted the average values of data in grid and computed the liquefaction probability model using the previously described data. This study performed logistic regression using various combinations of variables as listed in Table 10. If grid contains the mountain area, 760m/s, 0, and 50 are considered for V_{S30}, $\boldsymbol{D^{rock}}$, $\bar{\boldsymbol{N}}^{\boldsymbol{5m}}$, respectively. The effects of PGV, $\bar{N}^{z}$ for other depths and V_{SZ} for other depths are discussed in the subsequent section.

3.4 Results

This study considered numerous combinations of factors as shown in Table 10. These various models include factors from each of the three categories (ground intensity, soil intensity, and water contents), considering that the PGA is indispensable. These various models were evaluated using accuracy and Akaike's Information Criterion (AIC). The method for calculating accuracy is mentioned in Section 2.6. This time, various probability thresholds were used.

The Akaike's Information Criterion (AIC) was introduced by Akaike (1973) estimates the quality of each model and gives the goodness of fit of a model.

$$AIC = -2\ln(L) + 2n \tag{17}$$

where L is the maximum likelihood function for the model and n is the number of estimated parameters.

The estimated maximum accuracy and AIC values are presented in Table 10. Lower values of AIC correspond to better models. Generally, PGA is a representative earthquake load parameter, and $\bar{N}^{5m}$ is a parameter for soil strength. This study considers the Model 1 as a base model that consists of two variables: PGA and $\bar{N}^{5m}$. The base model has 67 values at the maximum accuracy and 1066.94 values in AIC. The model with PGA and V_{S30} (Model 5) has the maximum accuracy of 63 and an AIC value of 1178.51. and Model 4 has 68 values at the maximum accuracy and 1096.89 values in AIC. The model with PGA and D^{rock}. In addition, this study uses CTI and R^{river} to take into account the effect of water contents. Models 10 and 11 are to examine the effects of CTI and R^{river}. Model 10 and Model 11 have all the same variables, but Model 10 uses CTI and Model 11 uses R^{river}. Because Model 10 has higher maximum accuracy and a lower AIC value than Model 11, it can be concluded that CTI has more influence than R^{river}. According to the Table 10, this study selected the Model 10 as the best performing model which uses PGA, $\bar{N}^{5m}$, CTI, D^{rock} and V_{S30} as variables. Table 11 shows the coefficients of the best model.

Table 10 Models with various combinations of factors and their performance evaluation

Model number	Combination of factors	Maximum accuracy	AIC (Akaike Information Criterion)
1	PGA, $\bar{N}^{5m}$	67	1066.94
2	PGA, CTI	65	1163.05
3	PGA, R^{river}	54.5	1219.83
4	PGA, D^{rock}	68	1096.89
5	PGA, V_{S30}	63	1178.51
6	PGA, $\bar{N}^{5m}$, CTI	70.5	1041.18
7	PGA, $\bar{N}^{5m}$, R^{river}	66.5	1068.11
8	PGA, $\bar{N}^{5m}$, V_{S30}	74	1000
9	PGA, $\bar{N}^{5m}$, D^{rock}	70.5	1050.73
10	PGA, $\bar{N}^{5m}$, CTI, V_{S30}, D^{rock}	76	977.15
11	PGA, $\bar{N}^{5m}$, R^{river}, V_{S30}, D^{rock}	75	985.06
12	PGA, CTI, $\bar{N}^{5m}$, V_{S30}	75	987.96
13	PGA, CTI, V_{S30}, D^{rock}	70	1076.28
14	PGA, $\bar{N}^{5m}$, CTI, V_{S30}, D^{rock}, R^{river}	75.5	978.73

Table 11 Coefficients of the best liquefaction probability model

Variable	Coefficient	Unit
Intercept	-13.4407	--
PGA	49.0928	g
$\bar{N}^{5m}$	-0.2104	m
CTI	0.0948	--
V_{S30}	0.01302	m/s
D^{rock}	0.1177	m

Figure 17 shows accuracy values with probability thresholds for three example models: Model 1 (base); Model 9; and Model 10 (best). It can be observed that the accuracy values for Model 9 are greater than those for Model 1 at most of thresholds. The accuracy values for the best model is greater than those for the other two models at all thresholds.

This study evaluated the effect of different depths for averaging shear wave velocities (i.e., V_{S5}, V_{S10}, V_{S20}, and V_{S30}) for the best model. Figure 18 shows accuracy values of the best model with V_{S30} are greater than using other depths. Figure 19 shows the receiver operation characteristics (ROC) curve of this study, compared with that by the previous study (Zhu et al. 2017). This study calculated the receiver operation characteristics (ROC) curve and compared it with the previous study to evaluate the proposed liquefaction probability model. According to the Figure 19, this study's ROC curve is located in the upper part of the graph than the previous study's results, implying that the model proposed by this study performs slightly better than the previous study.

Figure 20 shows liquefaction probability maps using the best model and base model (Figure 20a and Figure 20b, respectively). Overall, the probability from the best model ranges from 0 to 0.7, and that from the base model ranges from 0 to 0.4. The best model produced higher probabilities in the area where most of sand boils are concentrated.

In order to examine the differences between the best model and base model, residuals were estimated as:

$$residual = \ln(P^{best}) - \ln(P^{base}), \quad (18)$$

where P^{best} is the probability from the best model and P^{base} is that from the base model.

Figure 21 shows a map of the residuals. The residual has ranges from -2.14 to 2.5. It is clearly observed that P^{best} is greater than P^{base} where many sand boils occurred. Therefore, the best model that proposed by this study is good to apply in Korea.

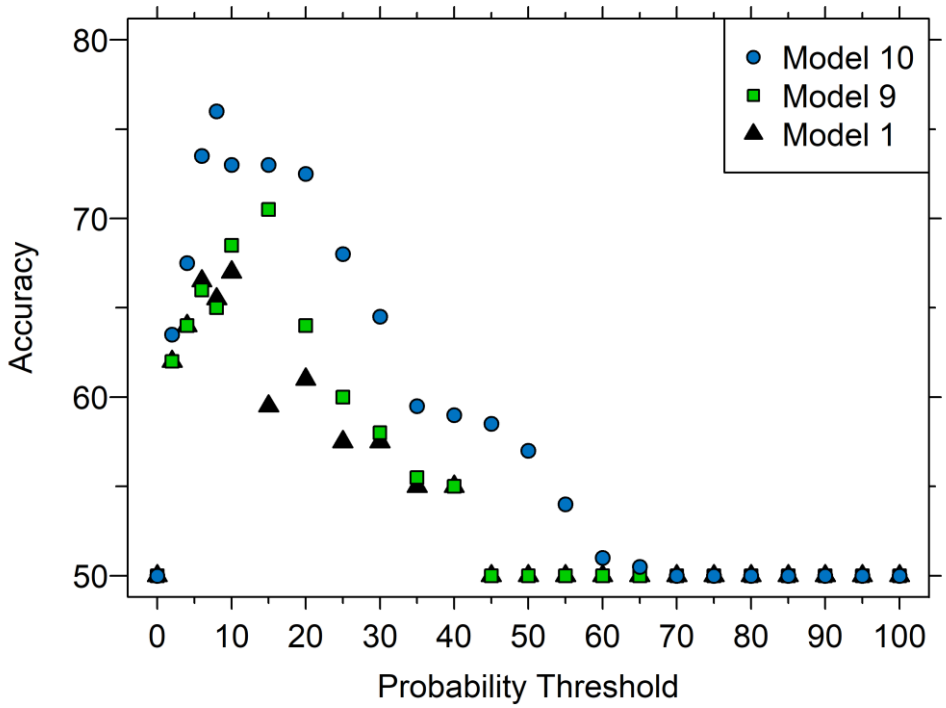

Figure 17 Accuracies of liquefaction probability models.

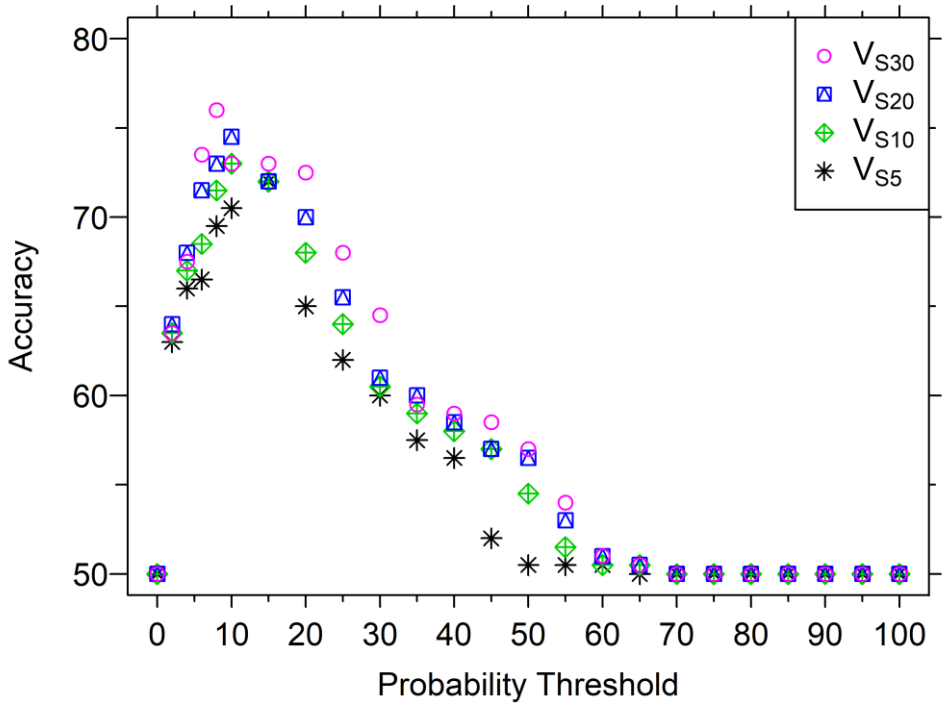

Figure 18 Accuracy values of the best model with various averaged shear wave velocities

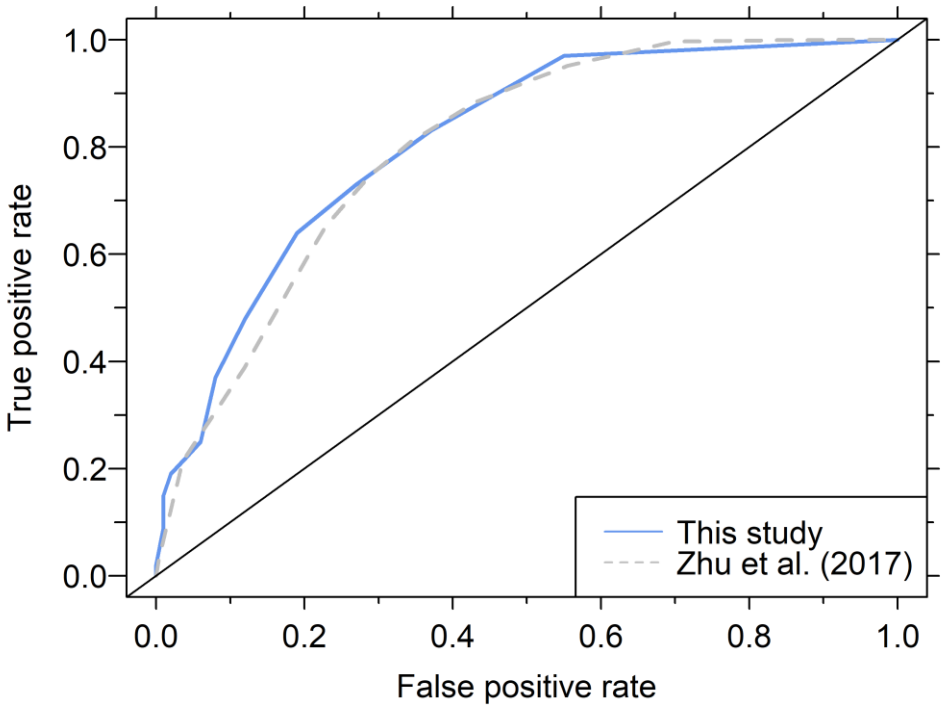

Figure 19 ROC curve of this study and previous study (Zhu et al. (2017) with a one-to-one line

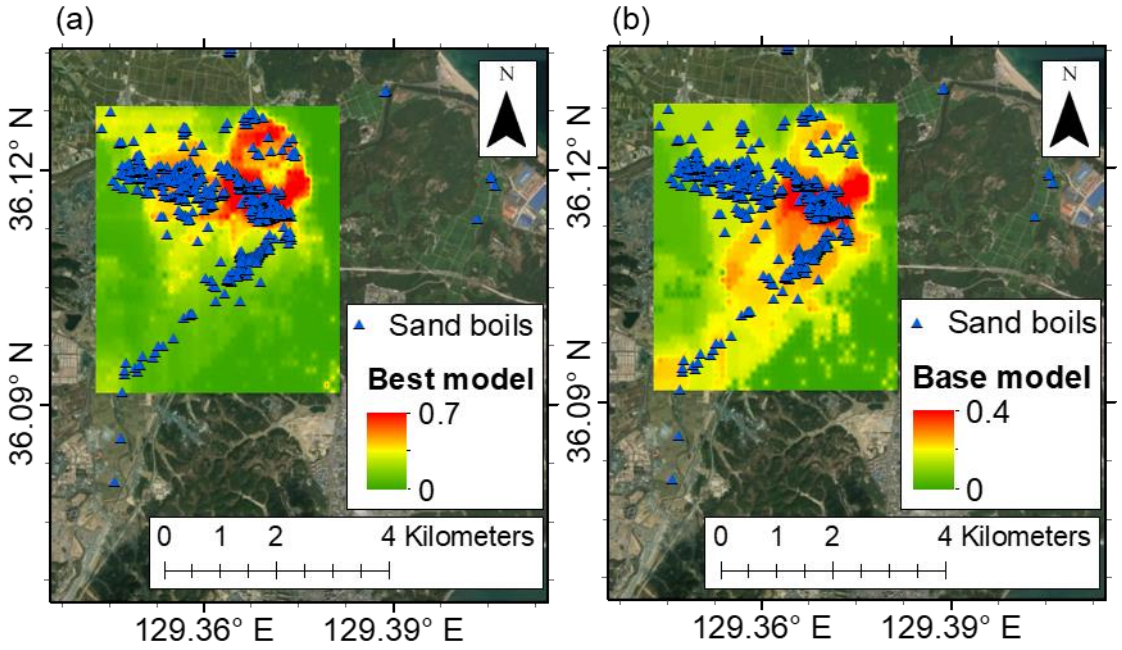

Figure 20 Maps of liquefaction probability based on (a) Model number 10 (best model), (b) model number 1 (base model)

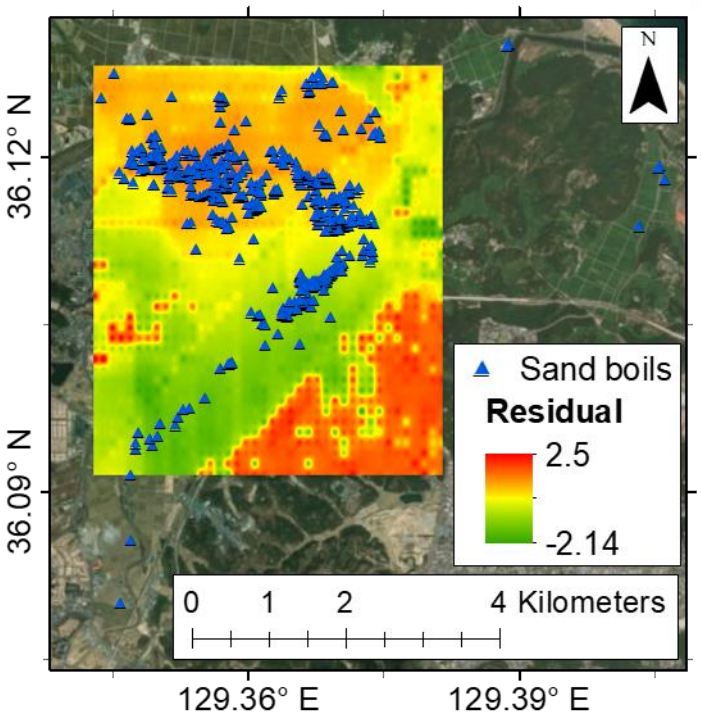

Figure 21 Map of residual best model and base model

4. CONCLUSIONS

This study calculated liquefaction severity indices such as Liquefaction Potential Index (LPI) and Liquefaction Severity Number (LSN) with approximately 2,000 SPT-N values from the Geotechnical Information Portal System, the National Disaster Management Research Institute, the Korea Meteorological Administration and local government offices and compared those with the locations of sand boils. This study computed LPI following the procedure proposed by Iwasaki (1978) and LSN based on the approach by Tonkin and Taylor (2013). LPI and LSN values were estimated at all the borehole locations. The spatial interpolation was conducted with the Inverse Distance Weighted (IDW) method to estimate LPI and LSN values for the areas where no borehole data are available. The estimated LPI and LSN values were highest in the center of the basin, which are consistent with spatial distribution of sand boil observations. For the statistical analysis this study used accuracy, the confusion matrix. This study created 1,600 grids within the study area. A confusion matrix was developed for the 1,264 grids excluding mountain areas. LPI has 69.5% and LSN has 67.5% accuracy values. It is worth noting that prediction of liquefaction using LPI is better than that using LSN for Korea. In addition, numbers of the grid with and without sand boils are used to calculate probability. The probability increases with LPI and LSN.

Furthermore, this study used the data for ground motion intensities, geological, and soil characteristics (i.e., peak ground acceleration (PGA), peak ground velocity (PGV), compound topographic index (CTI) from the digital elevation model (DEM), average SPT-N value for the top 5m soil deposits, distance to river near the locations of sand boil, V_{S30} and depth to rock). The $\bar{N}^{5m}$, V_{S30} and D^{rock}, which were obtained from the borehole data, were spatially interpolated using the KRIGING. The geospatial liquefaction probability model was derived through logistic regression. According to the various combinations of factors, this study selected the best model (top performing). In the best model, this study changed V_{S30} data to V_{S5}, V_{S10} and V_{S20} and found out V_{S30} performs better than the other factors. Therefore, this study's best model is based on PGA (from Shake Map), CTI, $\bar{N}^{5m}$, D^{rock} and V_{S30}. It has 76% maximum accuracy according to the probability threshold. This prediction performance is better than LPI and LSN. This study is based on the sand boil observations and geology and geotechnical data in Pohang. Therefore, caution is needed when applying LPI, LSN, and the proposed geospatial liquefaction model to other regions in Korea.

REFERENCES

Akaike, H. (1973). "Information Theory and an Extension of the Maximum Likelihood Principle." 199--213.

Boore, D. M., et al. (1997). "Empirical near-source attenuation relations for horizontal and vertical components of peak ground acceleration, peak ground velocity, and Pseudo-absolute acceleration response spectra." Seismological research letters **68**(1): 154-179.

Boulanger, R. and I. Idriss (2014). "CPT and SPT based liquefaction triggering procedures." Report No. UCD/CGM.-14 **1**.

Boulanger, R. W. (2003). "Relating K α to relative state parameter index." Journal of geotechnical and geoenvironmental engineering **129**(8): 770-773.

Boulanger, R. W. and I. Idriss (2007). "Evaluation of cyclic softening in silts and clays." Journal of geotechnical and geoenvironmental engineering **133**(6): 641-652.

Cetin, K. O., et al. (2004). "Seismically induced landslide at Degirmendere Nose, Izmit Bay during Kocaeli (Izmit)-Turkey earthquake." Soil Dynamics and Earthquake Engineering **24**(3): 189-197.

Cetin, K. O., et al. (2018). "Dataset on SPT-based seismic soil liquefaction." Data in brief **20**: 544-548.

Choi, S., et al. (2012). Active fault map and seismic hazard map.

Coduto, D., et al. (2011). Geotechnical engineering : principles and practices, 2nd ed. Upper Saddle River, NJ : Prentice Hall.

Gihm, Y. S., et al. (2018). "Paleoseismological implications of liquefaction-induced structures caused by the 2017 Pohang earthquake." Geosci. J.(6): 871-880.

Holzer, T. L., et al. (2006). "Liquefaction hazard mapping with LPI in the greater Oakland, California, area." Earthquake Spectra **22**(3): 693-708.

Idriss, I. (1999). "An update to the Seed-Idriss simplified procedure for evaluating liquefaction potential." Proc., TRB Worshop on New Approaches to Liquefaction, Pubbl. n. FHWA-RD-99-165, Federal Highway Administation.

Idriss, I. and R. Boulanger (2004). "Semi-empirical procedures for evaluating liquefaction potential during earthquakes." Soil Dynamics and Earthquake Engineering **1**: 32-56.

Idriss, I. M. and R. W. Boulanger (2008). Soil liquefaction during earthquakes, Earthquake Engineering Research Institute.

Iwasaki, T. (1978). A practical method for assessing soil liquefaction potential based on case studies at various sites in Japan. Proc. Second Int. Conf. Microzonation Safer Construction Research Application, 1978.

Iwasaki, T., et al. (1982). Microzonation for soil liquefaction potential using simplified methods. Proceedings of the 3rd international conference on microzonation, Seattle.

Kang, S., et al. (2019). "Earthquake-Induced Ground Deformations in the Low-seismicity Region: A case of the 2017 M5. 4 Pohang, South Korea, Earthquake." Earthquake Spectra.

KIGAM, K. I. o. G. a. M. R. (2018). "Earthquakes in the Southeast Korean Peninsula: Focusing on the 2016 Gyeongju and the 2017 Pohang Earthquakes."

Kim, H.-S., et al. (2018). "Geospatial assessment of the post-earthquake hazard of the 2017 Pohang earthquake considering seismic site effects." ISPRS International Journal of Geo-Information **7**(9): 375.

KMA , K. m. a. (2018). Analysis of Pohang earthquake report.

Liao, S. S. and R. V. Whitman (1986). "Overburden correction factors for SPT in sand." Journal of Geotechnical Engineering **112**(3): 373-377.

Maurer, B. W., et al. (2014). "Evaluation of the liquefaction potential index for assessing liquefaction hazard in Christchurch, New Zealand." Journal of geotechnical and geoenvironmental engineering **140**(7): 04014032.

Moss, R. E. S., et al. (2017). "Examining the discrepancy between forecast and observed liquefaction from the 2015 Gorkha, Nepal, earthquakes." Earthquake Spectra **33**(S1): S73-S83.

Robertson, P. (1990). "Soil classification using the cone penetration test." Canadian Geotechnical Journal **27**(1): 151-158.

Seed, H. B. and I. M. Idriss (1967). "Analysis of soil liquefaction: Niigata earthquake." Journal of the Soil Mechanics and Foundations Division **93**(3): 83-108.

Seed, H. B. and I. M. Idriss (1971). "Simplified procedure for evaluating soil liquefaction potential." Journal of Soil Mechanics & Foundations Div.

Seed, R. B., et al. (2003). Recent advances in soil liquefaction engineering: a unified and consistent framework. Proceedings of the 26th Annual ASCE Los Angeles Geotechnical Spring Seminar: Long Beach, CA.

Shepard, D. (1968). A two-dimensional interpolation function for irregularly-spaced data. Proceedings of the 1968 23rd ACM national conference, ACM.

Sonmez, B. and R. Ulusay (2008). "Liquefaction potential at Izmit Bay: comparison of predicted and observed soil liquefaction during the Kocaeli earthquake." Bulletin of Engineering Geology and the Environment **67**(1): 1-9.

Tokimatsu, K. and H. B. Seed (1987). "Evaluation of settlements in sands due to earthquake shaking." Journal of Geotechnical Engineering **113**(8): 861-878.

Tonkin and Taylor (2013). "Liquefaction Vulnerability Study." Earthquake Commission.

Van Ballegooy, S., et al. (2013). "LSN–a new methodology for characterising the effects of liquefaction in terms of relative land damage severity."

Van Ballegooy, S., et al. (2014). "Assessment of liquefaction-induced land damage for residential Christchurch." Earthquake Spectra **30**(1): 31-55.

Youd, T. L. and I. M. Idriss (2001). "Liquefaction resistance of soils: summary report from the 1996 NCEER and 1998 NCEER/NSF workshops on evaluation of liquefaction resistance of soils." Journal of geotechnical and geoenvironmental engineering **127**(4): 297-313.

Zhu, J., et al. (2017). "An updated geospatial liquefaction model for global application." Bulletin of the Seismological Society of America **107**(3): 1365-1385.

Zhu, J., et al. (2015). "A geospatial liquefaction model for rapid response and loss estimation." Earthquake Spectra **31**(3): 1813-1837.